Resolution and Precision of Fast Long-Range Terrestrial Photogrammetric Surveying Aimed at Detecting Slope Changes

Resolution and precision of fast, long range terrestrial photogrammetric surveying aimed at detecting slope changes

Arianna Pesci[1], Giordano Teza[2], Vanja Kastelic[3] and Michele M.C. Carafa[4]

[1]*Researcher, Istituto Nazionale di Geofisica e Vulcanologia, Sezione di Bologna, via Creti 12, I-40128 Bologna, Italy (Corresponding author). Email: arianna.pesci@ingv.it. ORCID: 0000-0003-1863-3132.*

[2]*Research Assistant, Department of Geosciences, University of Padua, via Gradenigo 6, I-35131 Padova, Italy. E-mail: giordano.teza@gmail.com. ORCID: 0000-0002-6902-5033.*

[3]*Researcher, Istituto Nazionale di Geofisica e Vulcanologia, Sezione Tettonofisica e Sismologia, Viale F. Crispi 43-45, 67100 L'Aquila, Italy. E-mail: vanja.kastelic@ingv.it. ORCID: 0000-0002-7751-0055.*

[4]*Researcher, Istituto Nazionale di Geofisica e Vulcanologia, Sezione Tettonofisica e Sismologia, Viale F. Crispi 43-45, 67100 L'Aquila, Italy. E-mail: michele.carafa@ingv.it. ORCID: 0000-0001-5463-463X.*

Abstract

Structure-from-Motion (SfM) is currently used for geological-geomorphological purposes under the condition that the modeling is based either on several ground control points (GCPs) well distributed in the scene or on Direct Georeferencing (DG). In emergency conditions and in presence of active morphodynamic processes, it could be unfeasible to use GCPs or DG. A study aimed at evaluating the quality of the results achievable by means of completely free SfM modeling of images taken from a distance of some hundred meters is shown here. It is based on an experiment with an artificial target and some surveys of a bedrock scarp, where resolution and precision are evaluated as empirical functions of distance and focal length, taking into account the issues related to the scale factor. The problems related to the recognition of localized surface changes by means of multitemporal surveys are also studied. The main result is that the free approach can really be used in geomorphological and seismotectonical surveying carried out in emergency conditions.

Subject Headings: Structure-from-Motion; Spatial Resolution; Precision; Change Detection; Slope Stability; Central Apennines.

1. Introduction

Structure-from-Motion (SfM) is increasingly used in geological and geomorphological surveying because it allows a fast and inexpensive generation of accurate photorealistic point clouds and digital models with the currently available computation resources (see e.g. Brunier et al. 2016; Smith et al. 2016). In case of good light conditions and absence of disturbances like vegetal cover, SfM is often used instead of the expensive Terrestrial Laser Scanning (TLS) because of similar performance (Nouwakpo et al. 2016; Teza et al. 2016; Pesci et al. 2018).

A fundamental step of the photogrammetric modeling is the bundle adjustment (BA), which consists in a simultaneous refinement of the 3D coordinates that describe the scene geometry, the camera positions, orientations and optical characteristics (Murtiyoso et al. 2018). The standard approach is based on block BA (Triggs et al. 2000), where the coordinates of several Ground Control Points (GCPs) measured by means of GNSS and/or total station, and also recognized in some input images, are incorporated into the BA procedure. The achievable precision is directly related to the number of GCPs and their distribution. In particular, a uniform and dense GCP spatial distribution is required in those cases where highly accurate products are needed (Caroti et al. 2015; Tonkin and Midgley 2016; Al-Halbouni et al. 2017). A direct access to the surveyed surface is required, but it could be difficult or hazardous in unstable slope areas. Moreover, multipath effects and/or limited satellite visibility can affect the GNSS-based measurement of GCPs in the case of a vertical rock cliff (Jaud et al. 2016). Finally, the time-intensive nature of GCP collection requires a balance between GCP quantity and survey quality. For example, several working hours are necessary to acquire 20-30 GCPs by means of GNSS measurements on a ~2 ha surface.

Sometimes, not enough reliable GCPs can be measured. In these cases, the direct georeferencing (DG) can be used (Turner et al. 2014). Such an approach is particularly

suitable for aerial SfM because an Unmanned Aerial System (UAS) is typically equipped with a GNSS receiver. In this case, the camera positions (positions and orientations if an Inertial Measurement Unit, IMU, is also available), defined with respect to a suitable reference system, are used in order to provide a georeferenced point cloud. The DG workflow seems to lead to higher errors compared to GCP-based modeling. Nevertheless, an adequate DG workflow can produce topographic data with sufficient quality for some applications even if low cost UAS and SfM-photogrammetry package are used (Carbonneau and Dietrich 2017). Finally, the cost of instruments necessary for a DG-based survey is an order of magnitude lower than the one necessary for a GCP-based survey (~2,000 $ instead of ~15,000-20,000 $).

The fact that a high precision geodetic survey should be based on GCPs or at least on DG is a shared and well-founded opinion. On the contrary, point clouds and digital models obtained by means of a completely free SfM modeling are considered to be suitable for representation purposes but unsuitable for quantitative analyses because of deformations with respect to the true shape, incorrect scale factor (SF) and lack of georeferencing. Since in some cases the surveying in emergency conditions could be incompatible with GCPs or also DG, it is important to understand what can be achieved in these cases. For this reason, the issues related to a completely free SfM surveying and modeling of a rock cliff are faced in this paper. In particular, the answers to these important questions are proposed: Can a completely free SfM modeling be used be used in geomorphological and seismotectonic surveying, at least in emergency conditions? What is a possible solution of the SF problem? What are reasonable estimates of resolution and precision? What conditions should the observed rock cliff satisfy in order to have meaningful results from multitemporal observations?

2. Preliminary experiment with an artificial target

This experiment was carried out in order to evaluate the resolution, i.e. the size of the smallest feature that can be detected and measured, of SfM modeling as a function of the acquisition distance and technical specification of the used camera.

The artificial target is a white rectangular planar wood panel whose base and height are 1 m and 0.3 m respectively (Fig. 1a). Some 0.2 m high vertical black rectangular elements are placed on the panel. On the left side there are ten elements whose widths range from 1 mm to 10 mm, and on the right side there are ten elements between 11 mm and 20 mm. The color contrast between black vertical elements and white background facilitates their recognition. The target was placed on a masonry wall in order to integrate it within a more extended environment.

[Figure 1]

The images were taken by means of a Nikon D3300 camera, equipped by a lens which allows the choice of a focal length in the range 55-300 mm, whose main technical specification are summarized in Table 1. The experiment layout is shown in Fig. 1b. The camera was placed along five lines parallel to the masonry wall at distances of 10 m, 20 m, 30 m, 40 m and 50 m. Seven evenly spaced points were considered for each line and three images were taken from each point by using three different focal lengths *f*, i.e. 55 mm, 102 mm and 210 mm. The image acquisition was carried out by moving parallel to the target as in the case of terrestrial surveying of a slope. The camera's optical axis was always aimed at the target in order to ensure that it was in the center of each image. In this way, the survey was very like to the observation of a natural surface. The price to pay was a changing acquisition distance along each line (10-11.9 m, 20-23.8 m, 30-35.7 m, 40-47.5 m, 50-59.4 m, with mean distances of 10.8 m, 21.6 m 32.4 m, 43.2 m and 53.9 m respectively).

For each line and each *f*, a dense point cloud was generated from the corresponding seven images by using PhotoScan (now called Metashape, Agisoft 2020). The image alignment was carried out with the full size images, without subsampling, by choosing the

option “High accuracy” in PhotoScan. Similarly, the choice “Ultra High” for quality led to a dense point cloud generation based on full size images. Moreover, in order to reduce noise and keep the small details at the same time, the chosen option for depth filtering was “Moderate”. A total of 15 point clouds were obtained. Each point cloud was inspected by using PolyWorks (Innovmetric 2020) in order to recognize and evaluate the black vertical elements. These elements were automatically selected because they are dark color features on a light background. Since the *i*-th element has the width of *i* mm and the difference between the *i*-th and the (*i*+1)-th element is 1 mm, if the element *i* can be seen but its width cannot be measured and the element *i*+1 is visible and its width can be measured, an estimate of the point cloud resolution, i.e. the size of the smallest object that can be discerned, is *i*+0.5 mm.

The results are shown in Fig. 2, where the resolution vs. acquisition distance *d* is shown together with the Ground Sampling Distance (GSD), i.e. the distance between the centers of two adjacent pixels measured on the observed surface, namely the image resolution, vs. *d*. It is $GSD = p\,d\,/\,f$, where *p* is the size of the single pixel of the sensor. In order to show the ratio between resolution and GSD by means of only a sequence of points and better evaluate the ratio between the point cloud resolution and the GSD, the case $f_0 = 55\,\text{mm}$ is used as a reference; the results for $f_1 = 102\,\text{mm}$ and $f_2 = 210\,\text{mm}$ are taken into account by means of the normalized distance $d_{Ni} = d\,f_0\,/\,f_i$.

The average ratio between resolution and GSD is ~2.5. This is the main result of the preliminary experiment. It is important to point out that a resolution equal to the GSD is not expected and is not possible. Even if a high quality lens is used, two images related to a same area but taken from two different positions cannot have a perfect pixel-by-pixel match. This is like the case of a TLS, whose resolution is not equal to the sampling step (Lichti and Jamtsho 2006; Pesci et al. 2011). Another similarity is the fact that the probability of reacquisition of a same point in two scans carried out with the same parameters is very low. The data provided

by a TLS instruments have an area nature, not a punctual one, i.e. a point in the same area, not the same point, is acquired in a second scan.

[Figure 2]

[Table 1]

It is important to note that: (1) the target is composed of dark elements with clear boundaries on a white planar background in order to allow a quick and easy recognition of these elements on the point clouds; (2) the distribution of the element widths is discrete; (3) the range of acquisition distances is no more than 10-50 m. For all these reasons, the fact that the point cloud resolution is ~2.5 times the GSD, is not a general result but is rather a limit value for the resolution that can be reached under optimal conditions in which disturbances due to complex morphologies and light problems are almost absent. Since the GSD linearly increases with the distance, it is reasonable to assume that this result can be extrapolated to distances greater than 50 m under the condition that a flat surface is observed with optimal lighting. For a general surface, the result is a lower limit of the resolution. For this reason, it is called resolution limit (RL). Possible changes and differences between models that are lower than such a limit cannot be accepted, but should be considered to be negligible instead. It is important to note that the GSD, even if it is not the resolution of the final 3D object (point cloud or model), constrains this parameter. The Modulation Transfer Function (MTF) of an imaging system is a measurement of its ability to transfer contrast at a particular resolution from the observed object to the image. Although a true MTF estimation was not carried out, the experiment provided some information about it. The RL roughly corresponds to the spatial frequency at which the MTF is 50%. Moreover, the result $RL \sim 2.5\,GSD$ means that the spatial frequency limit is $\sim 0.8\,f_N$, where $f_N = 1/(2GSD)$ is the Nyquist frequency, i.e. half the sampling frequency.

3. Geological setting

Mountain slopes in an active tectonic setting are exposed to different processes responsible for their long-term morphology. Aside from active faulting and other form of coseismic displacement during an earthquake, active faults exhibit also afterslip and, in some cases, aseismic creep in the interseismic periods. Moderate-to-strong earthquakes perturb the dynamic equilibrium of a mountain slope also through shaking-induced triggering of mass movement. Gravitational processes are also well documented in tectonically active regions (Baroň et al. 2016). Often, effects of reactivation of tectonic faults act on mountain morphology. Besides tectonics, there are several exogenic processes contributing to mountain morphologies, such as weathering, mass wasting, erosion and deposition. These processes are mainly related to gravity and lateral topographic gradients. Therefore, the detection of morphological changes and related rates is important to determine areas prone to deformation. Ultimately the goal is to properly model the observed variations to their causative factors.

[Figure 3]

The central Apennines are a mountain chain composed of individual NW-SE oriented slopes separated by karstic plateaus, glacio-fluvial valleys and fluvio-lacustrine basins. The generally NW-SE oriented bedrock scarps (BSs) positioned at various heights along the individual mountain slopes are important geomorphic features of this area. These structures are often thought to be a direct surface exposure of the region seismogenic faults and their heights are directly associated with earthquake surface faulting. Generally, the other processes known to affect mountainous morphology are neglected in the studies about central Apennines. It was recently shown that the exposure of these BSs occurs at fast rates and without earthquake slip due to not yet very well understood mechanisms, probably driving BS exposure in interseismic times (Kastelic et al. 2017). Moreover, during earthquakes, gravity and earthquake shaking-induced movement on pre-existing discontinuities significantly influence the coseismic surface deformation (Di Naccio et al. 2019). These evidences suggest

that a more specific study of terrain movements have to be considered to better quantify the non-tectonic contribution, which should be quantified and eventually subtracted from the estimates of tectonic deformation. This issue has important implications in different aspects, for example in seismic hazard studies where only the long-term seismogenic component of the overall deformation is needed, thus all other components of the total deformation pattern need to be removed.

Campo Felice (Fig. 3) is a BS in the central Apennines characterised by a significant lowering rate without seismogenic component (Kastelic et al. 2017). The surveys were aimed at studying a large portion of this BS and its underlying mountain slope, where change rates in the range between ~1 cm/a and ~10 cm/a are typically expected. Therefore, the surveying method should be able to detect these changes. A possible solution is the ground-based interferometric Synthetic Aperture Radar (SAR), which allows the real-time detection of millimetric changes with pixel resolution of half meter (Ferrigno et al. 2017), but this is an expensive technique. SfM seems the most appropriate choice due to its performance and low cost and the need to develop time series of point displacements and models of differential movements on the BS.

4. Surveys and Results

4.1 Surveys

The rock cliff chosen for in situ SfM experiment was also surveyed by means of TLS technology in order to obtain a reference metric point cloud with the correct verticality. An Optech ILRIS-3D ER instrument was used from ~250 m mean distance (Fig. 4). An inspection of the point cloud led to basic information as slope inclinations and distances between some areas of the cliff. TLS is an expensive tecnique, but this measurement was carried out once and for all.

[Figure 4]

206 The SfM surveys were performed in April 2018 by using a Nikon D3300 camera. The
207 images were acquired with three *f* values: 55 mm, 110 mm and 220 mm. Each *f* was set by
208 acting on the camera lens ring (among the values written on the ring, there are 55 mm, 102
209 mm, 110 mm, 210 mm and 220 mm). Since possible changes in *f* can have a significant
210 impact the model fidelity, for each image the Exif data were read in order to check the actual
211 *f*. For each *f*, two sets of 30-44 images, depending on *f*, were acquired from the paved road
212 that runs roughly parallel to the BS at ~250 m distance from the road to this BS. Details on
213 data acquisition and processing are summarized in Table 2. The photographer walked for
214 ~300 m along the road acquiring an image every 10 m to have a good spatial coverage and
215 image overlap and repeated the procedure as she turned back. The camera was always aimed
216 with parallel optical axes. The surveys were repeated in March 2019 to provide multitemporal
217 data.
218 [Table 2]
219
220 ***4.2 Photogrammetric modeling and resolution evaluation***
221 The photogrammetric modeling was carried out by using PhotoScan with a free-network BA
222 approach. Before the dense point cloud generation, the image alignment was checked and,
223 where necessary, corrected. The options for image alignment ("High accuracy") and dense
224 point cloud generation ("Ultra High quality" and "Moderate depth filtering") were the same as
225 those for the above described experiment (see Table 2 for more inormation).
226 Figure 5 shows the 55 mm point cloud together with the boundaries for the three *f*. The
227 longer the focal length, the smaller the modelled area. The area of interest is the area where
228 there is the transition between rock and debris, i.e. the BS contact with alluvium/colluvium
229 (Section 3). It corresponds to the area covered by the 220 mm point cloud.
230 [Figure 5]

In order to obtain metric objects, the point clouds were scaled by means of the polylines method (Pesci et al. 2016). It is based on the choice of some common homologous points (e.g. morphological details) recognized in all point clouds and on the calculation, in each point cloud, of the length of the closed polyline connecting these points. The recognition of homologous point is quite simple because the SfM-based point clouds are photorealistic. Let L_i be the polyline length related to the point cloud *i*. In order to express the point cloud *j* in the same scale of the point cloud *i*, the scale factor $SF_{ji} = L_i / L_j$ must be used. Therefore, it is $S_{ji} = S_j SF_{ij}$, where S_{ji} indicates an object initially defined in the scale *j* changed to the scale *i*. If *i* is metric, also *j* becomes metric. The SfM point clouds were made metric by extracting from the TLS point cloud the polyline that correspond to the SfM ones. This final task was not as easy as the previous ones because the radiometric information of the TLS point cloud is the intensity in the near infrared band and the recognition of homologous points is not trivial. In order to have meaningful results, the polyline should roughly coincide with the boundaries of the area of interest. The problems related to the choice of the closed polylines used to evaluate the scale factor are discussed in detail in the Online Supplementary Material.

The metric point clouds can be registered onto the same reference frame by means of rigid body transformations in order to allow their comparison. Like the above described approach to data scaling, the SfM point clouds were registered between them. A 110 mm point cloud was aligned to the TLS one after this, and the resulting rigid body transformation was applied to all SfM point clouds to allow the data comparison. Data scaling, registration and comparison were carried out by using PolyWorks. In particular, the comparison between two point clouds was carried out by generating a 2.5D model from the reference one and measuring the distance between each element of the second point cloud and this model. The statistical data analysis was carried out with Origin package by OriginLab.

A test of repeatability was carried out. The maps of differences between each pair of point clouds related to the same *f* are shown in Fig. 6: 55 mm (Fig. 6a), 110 mm (Fig. 6b) and 220 mm (Fig. 6c). In order to facilitate the result interpretation, areas affected by vegetation coverage were excluded from the analysis. The results are summarized in Table 3.

[Figure 6]

[Table 3]

The statistical analysis of the differences between each pair of point clouds related to the same *f* shows that, with the exception of the 55 mm case, the distribution has smaller standard deviation (SD) as *f* increases, as expected (Fig. 7a). Even if it is quasi-symmetric and almost zero-centered, this distribution typically is not normal since it has high kurtosis and, therefore, the probability mass is concentrated around the mean but there are occasional values far from the mean. In the 55 mm case, the values are not distributed around zero but seem to come from the sum of two symmetric distributions. This result can be related to the fact that the area taken in a single 55 mm image is relatively wide and, because of the slope angle of the cliff, different zones could be observed under very different conditions. The local distance and incidence angle can change, leading to different size and shape of the surface corresponding to a single pixel and making the registration harder. The corresponding map of differences (Fig. 6a) shows a pattern that seems to indicate an imperfect alignment, even if the values are small in consideration of the acquisition distance. A higher *f* lead to a lower field of view and, therefore, to a lower within-image variability of distance and incidence angle. The experiment with an artificial target described in Section 2 shows that the RL is about 2-3 times the GSD. If the comparison between two point clouds provides differences smaller than this limit, these differences are considered to be negligible and therefore rejected. For 250 m acquisition distance, the estimated RLs are 70 mm, 40 mm and 35 mm for 55 mm, 110 mm and 220 mm focal length respectively, whereas three times the standard deviations of the

differences are 60 mm, 35 mm and 25 mm respectively. Therefore, the detected differences are negligible and the repeatability of the results is confirmed.

[Figure 7]

The comparisons between point clouds obtained by means of different *f* is shown in Fig. 6: 55 mm vs. 110 mm (Fig. 6d); 55 mm vs. 220 mm (Fig. 6e) and 110 mm vs. 220 mm (Fig. 6f), and are summarized in Table 3. Like the case of repeatability test (Fig. 6a-c). there are systematic effects in case of comparisons with respect to the 55 mm point cloud. No systematic effects are observed for other point clouds and no patterns appear. Moreover, it should be noted that similar results are obtained whatever the point cloud for a given *f* is used.

A statistical analysis of differences between the point clouds obtained with different *f* showed a poor agreement between the 55 mm data and the ones related to higher *f* (Fig. 7b). The SfM models obtained through images with higher *f* offer a level of precision that can be though reliable and statistically representative of the process responsible for the possible differences detected. These results, like the ones shown in Fig. 7a, show that significantly better results are obtained for 110 mm and 220 mm with respect to 55 mm.

4.3 Analysis of multitemporal data

Scaling and registration of the 2019 point clouds were carried out with respect to a 2018 point cloud obtained from 110 mm images. Preliminary results on detection of changes occurred in the time span 2018-2019 for a *f* of 110 mm are shown in Fig. 8. At the acquisition distance (~250 m), no real movements along the contact between the rock and the deposit were observed. Faint traces of these movements can be seen, but they are below the RL, i.e. 30-40 mm at such a distance (Fig 8.d). On the contrary, significant differences were detected about the deposit accumulation on the wedges. Differences due to the vegetation cover also appear.

These results testify that the proposed simplified approach without GCPs and DG, although conceived for observations in emergency conditions, can recognize and quantify the

306 natural processes that affect a mountain slope if they involve a limited area of this slope.
307 Everything suggests that the time passed between the two multitemporal observations is too
308 short to allow the quantification of movements along the contact between rock and deposits.
309 In particular, Kastelic et al. (2017) estimated the lowering of the detrital part besides the BS
310 by means of direct in situ measurements, providing values of the order of 10 mm/a. Therefore,
311 a time span of about four year is needed to observe surface variations.
312 [Figure 8]
313
314 **5. Discussion**
315 The discussion focuses on the results that can be obtained by means of SfM without GCPs
316 and DG in the case of a rock cliff observed from 250 m, mainly in terms of spatial resolution
317 and minimum detectable magnitude of changes.
318 Some software manufacturers (e.g. Agisoft) claim that the typical resolution of a
319 photogrammetric model is 2-3 times the GSD of the taken images. Obviously, any statement
320 by a manufacturer must be verified under operating conditions. On the one hand, the assertion
321 about the resolution seems to be confirmed by the results of the preliminary experiment. The
322 value found in the experiment was ~2.5 times the GSD. On the other hand, it should be noted
323 that these results were obtained in 2D conditions, with a smooth surface and a high color
324 contrast between recognized elements and background. Therefore, this result is not general
325 and cannot be directly extrapolated to rough surfaces and/or cases where there is not enough
326 color contrast because of the color of the objects or the light conditions. In these cases, this is
327 simply a lower limit of the resolution. In particular, some experimentations on 3D natural
328 surfaces are required.
329 Several authors compared the SfM and TLS performance in terms of resolution and
330 accuracy, both for architectural/cultural heritage documentation (see e.g. Teza et al. 2016) and
331 geological/geomorphological survey (Nouwakpo et al. 2016). In particular, the last paper

showed that TLS and SfM have similar performance at least if the vegetal cover is negligible and several GCPs are used. Performance of SfM was evaluated e.g. by Caroti et al. (2015), which found that, in the observation of a façade, the root mean square error (RSME) ranges from 3 to 5 times the GSD in the case of free-net BA and ranges from 2 to 4 times the GSD if 6-12 GCPs evenly distributed on such a façade are used to constrain the BA.

This article deals with the observation of a rock cliff whose extension is some tens/hundreds m^2 where targets for total station or GNSS receivers cannot be placed. If a high extension surface is observed, the use of a suitable number of GCPs is strongly recommended because a free-network BA in this case could provide not more than preliminary values. A possible solution of the issues related to difficult or impossible access to a slope is the use of a reflectorless total station to accurately locate some features that can be recognized on the observed scenario (e.g. corners of natural or artificial objects). In this case, for mid acquisition distances the error is not significantly higher than the one of a GNSS survey carried out with receivers mounted on topographical tripods (Beshr and Elnaga 2011). However, such an instrument should be available for each survey, which is a problem for users whose available economic resources are limited or fast measurements and results are needed. The measurement campaigns were deliberately carried out without camera pre-calibration in order to show the quality of the results obtainable in emergency conditions and without any preparation. However, it should be noted that a camera pre-calibration is generally recommended.

The data acquisition was carried out with different focal lengths and, therefore, different GSDs. The results obtained in the 55 mm case (GSD of 18 mm at 250 m), are not adequate. The repeatability is not good; the distribution of the differences between two point clouds obtained in similar conditions is bimodal and not centered in zero. The pattern of differences shows that the bimodality of the distribution is mainly due to issues in data registration. In other words, the quality of the modeling aimed at aligning the point clouds is conditioned

358 from an unsuitable choice of the focal length, also taking into account the image field of view
359 and the slope angle of the cliff. All these issues do not appear if *f* is 110 mm or 220 mm,
360 where the GSD is 9 mm and 4.5 mm respectively. Therefore, the results suggest the choice of
361 the lens on the basis of the magnitude of the changes that should be detected. Finally, it
362 should be noted that, in case of observation of a subvertical cliff with 55 mm *f*, the
363 registration is easy and accurate (Pesci et al. 2019).

364 If the aim is the detection of possible changes occurred between two multitemporal
365 surveys and the SD of each model is σ, the SD of the difference is $\sqrt{2}\sigma$. The results show that
366 changes higher than 30-40 mm for a distance of ~250 m can be observed.

367 The used camera is a prosumer device, i.e. a mid-cost camera. Its crop factor (CF) is 1.5
368 (Table 1). It is commonly defined as $CF = diag_{35} / diag_S$, where $diag_{35}$ is the diagonal length
369 of a standard 35 mm photographic film, where $diag_{35} = 43.3\,\text{mm}$ for a 3:2 aspect ratio (36
370 mm x 24 mm sensor size) and $diag_S$ is the diagonal length of the specific sensor (in mm). A
371 professional full frame camera is characterized by $CF = 1$. A high CF leads to an excessive
372 squeezing of the pixel data on a small size sensor and, therefore, a low Signal-to-Noise Ratio
373 (SNR) and a low field of view, depending on focal length. If the CF increases, the other
374 factors and parameters being equal, the actual resolution of an image is worsened. This fact
375 should be taken into account if a camera mounted on a low cost UAS is used because the CF
376 could reach 4 or also 5.

377 A criticism can be made about the fact that the obtained results have area nature and, in
378 particular, do not have point nature. This is not a problem because the comparison between
379 point clouds for geological/geomorphological purposes is always based on comparisons
380 between areas and is never based on a direct comparison between points. For example, the
381 calculation of the displacement field from multitemporal point clouds by means of the
382 piecewise alignment method (Teza et al. 2007) and the correlation between digital

orthoimages generated from SfM-based point clouds (Travelletti et al. 2013) have area nature. If the aim is to evaluate volumetric changes, the calculation is, a fortiori, based on comparison between corresponding areas or between an area and a reference plane. In all cases, a single point is never considered.

Another criticism can be made with regard to the use of TLS data for the SF computation. This seems to contradict the claimed low cost of the procedure. However, the TLS-based point cloud, or a SfM-based point cloud generated by using several GCPs, is required once and for all and no further expensive surveys are required.

The polyline-based procedure aimed at providing the SF could also be used in those cases where no reliable reference models are available. For example, Google Earth (GE) imagery could be used to estimate the SF. However, the GE images are not orthorectified and, moreover, no public information about the data lineage and the procedures of data processing is available. No more than a first, rough estimate of the SF can therefore be obtained. Moreover, such a preliminary SF could be obtained under the condition that GE images having a relatively high resolution are available and that the rock cliff is not sub-vertical. In a metropolitan area the positional accuracy, expressed in terms of RSME, is typically in the range 0.7-1 m, which is sufficient for deriving ground truth samples, measurements, as well as large-scale maps (Pulighe at al. 2017), but in a rural area the RMSE can reach 5 m (Paredes-Hernandez et al. 2013). Therefore, in large part of the mountain areas the GE image resolution does not allow a preliminary SF estimation. A quasi-accurate SF could be obtained if 30 cm resolution digital orthoimages obtained from WorldView-3 satellite data (Vajsová et al. 2015) or 50 cm resolution orthoimages from Pléiades 1A/1B (Agrafiotis and Georgopoulos 2015) are used instead. This because orthorectified data having well defined precision and resolution are used and elevation data are embedded in a GeoTIFF file, allowing better recognition of homologous points.

In order to exclude possible systematic errors or distortions due to photogrammetric modeling, a final check was carried out by comparing the SfM point clouds and a reference TLS survey (Fig. 9). The difference maps show the absence of systematic errors for *f* of 110 mm and 220 mm. In the 55 mm case the differences range in the interval ±0.06 m and describe a pattern distributed along the diagonal of the surface.

[Figure 9]

In active tectonic studies it is important to properly quantify the seismogenic deformation, discarding any other process that could contribute to the short- and long-term landscape shaping. For this scope a cost- and time-effective method able to guarantee good resolution power is suitable for the surveying of surface deformations along BSs and mountain slopes both in coseismic and interseismic conditions. The proposed SfM models offer a chance to construct a database of BSs (and mountain-slopes) evolution through time, thus allowing to quantify and compare the spatially variable exposure rates. An analysis of multitemporal data collected in 2018 and 2019 confirms the results about precision and accuracy that can be reached with the proposed approach. Changes higher than the RL (30-40 mm at ~250 m distance) can be easily detected, whereas no more than faint traces of possible incipient changes can be detected along the contact between the rock and the deposit, where the velocity is ~10 mm/a. Therefore, the proposed approach can be used in emergency cases (earthquakes, landslides, volcanic eruptions) when easy-to-manage instrumentation and reliable results are equally needed.

Since a true georeferencing is not carried out, the completely free approach can be used only if the unstable area is a portion of the observed scene. In this case, the multi-temporal models can be co-registered on the basis of the stable parts of the rock cliff, provided that they surround the unstable areas. Even if this condition is often satisfied, this fact leads to an objective limitation of the proposed approach.

The time necessary to carry out the SfM survey was about 0.5 h and the polyline-based point cloud scaling required about 1 h. The computation times summarized in Table 2 show that the complete data processing (point cloud generation and scaling) of 220 mm data required about 5 h in the case of a notebook equipped with an Intel Core i7, 2.40 GHz CPU and 16 Gb RAM. Therefore, the procedure can be really used in emergency conditions.

6. Conclusions

The feasibility of terrestrial SfM surveys without GCPs and DG aimed at evaluating slope movements from distances of hundreds of meters was investigated by means of an experiment with an artificial target and in situ multitemporal surveys in Central Apennine area, Italy. Three different focal lengths (55, 110 and 220 mm) were considered and the point clouds were scaled on the basis of TLS data.

The results shown that there is a resolution limit, which is ~2.5 times the GSD. In particular, for ~250 m acquisition distance, the data obtained with focal lengths of 110 mm and 220 mm are widely comparable to each other and allow the observation of deformation patterns of at least 30-40 mm under the condition that there are localized unstable areas in a relatively stable cliff. The results prove the effectiveness of the used approach in surveying of mountain slopes in emergency conditions where the standard technique (modeling based on GCPs or at least DG) cannot be used.

Acknowledgments

This study was funded by Project MIUR-FIRB "Abruzzo", code RBAP10ZC8K_003 and Project "Fondo Integrato Speciale per la Ricerca – FISR 2016", Task 2. The authors wish to tank Massimo Bacchetti (University of Bologna, Department of Physics) for the help in target realization.

The authors wish to dedicate this article to the memory of Enzo Boschi (1942-2018).

Notation

The following symbols and acronyms are used in this paper:

BA: bundle adjustment;

BS: bedrock scarp;

CF: crop factor;

f: focal length;

f_N: Nyquist frequency;

GCP: Ground Control Point;

GNSS: Global Navigation Satellite System;

GSD: Ground Sampling Distance;

MTF: Modulation Transfer Function;

p: pixel size;

RL: resolution limit;

σ: standard deviation;

SF: scale factor;

SfM: structure-from-motion;

TLS: terrestrial laser scanning;

Online Supplemental Material

Quality of the scale factor as a function of polyline size.

Data Availability Statement

Some or all data, models, or code that support the findings of this study are available from the corresponding author upon reasonable request.

485 **References**

486 Agisoft. 2020. “Metashape web page.” Accessed February 7, 2020. http://www.agisoft.com.

487 Agrafiotis, P. and A. Georgopoulos. 2015. “Comparative assessment of very high resolution
488 satellite and aerial orthoimagery.” *Int. Arch. Photogramm. Remote Sens. Spat. Inf. Sci.*, XL
489 (3/W2). https://doi.org/10.5194/isprsarchives-XL-3-W2-1-2015.

490 Al-Halbouni, D., Holohan, E., Saberi, L., Alrshdan, H., Sawarieh, A., Closson, D., Walter,
491 T.R. and T. Dahm. 2017. “Sinkholes, subsidence and subrosion on the eastern shore of the
492 Dead Sea as revealed by a close-range photogrammetric survey.” *Geomorphology*, 285, 305-
493 324. https://doi.org/10.1016/j.geomorph.2017.02.006.

494 Baroň, I., Plan, L., Grasemann, B., Mitrovič, I., Lenhardt, W., Hausmann, H. and J. Stemberk.
495 2016. “Can deep seated gravitational slope deformations be activated by regional tectonic
496 strain: First insights from displacement measurements in caves from the Eastern Alps”.
497 *Geomorphology*, 259, 81-89. https://doi.org/10.1016/j.geomorph.2016.02.007.

498 Beshr, A.A.A. and I.M.A. Elnaga. 2011. “Investigating the accuracy of digital levels and
499 reflectorless total stations for purposes of geodetic engineering.” *Alex. Eng. J.*, 50 (4), 399-
500 405. https://doi.org/10.1016/j.aej.2011.12.004.

501 Brunier, G., Fleury, J., Anthony, J.E., Pothin, V., Vella, C., Dussouillez, P., Gardel, A. and E.
502 Michaud. 2016. “Structure-from-Motion photogrammetry for high-resolution coastal and
503 fluvial geomorphic surveys.” *Géomorphologie*, 22 (2), 147-161. https://doi.org/10.1007/978-
504 3-319-58304-4_9.

505 Carbonneau, P.E. and J.T. Dietrich. 2017. “Cost-effective non-metric photogrammetry from
506 consumer-grade sUAS: implications for direct georeferencing of structure from motion
507 photogrammetry.” *Earth Surf. Proc. Land.*, 42, 473-486. https://doi.org/10.1002/esp.4012.

508 Caroti, G., Martínez-Espejo Zaragoza, I. and A., Piemonte. 2015. “Accuracy assessment in
509 Structure from Motion 3d reconstruction from UAV-born images: the influence of the data

processing methods." *Int. Arch. Photogramm. Remote Sens. Spat. Inf. Sci.*, XL (1/W4), 103-109. https://doi.org/10.5194/isprsarchives-xl-1-w4-103-2015.

Di Naccio, D., Kastelic, V., Carafa M.M.C., Esposito C., Millilo, P. and C. Di Lorenzo. 2019. "Gravity versus Tectonics: the case of 2016 Amatrice and Norcia (central Italy) earthquakes surface coseismic fractures." *J. Geophys. Res.: Earth Surface*, 124 (4), 994-1017. https://doi.org/10.1029/2018JF004762.

Ferrigno, F., Gigli, G., Fanti, R., Intrieri E. and N. Casagli. 2020. "GB-InSAR monitoring and observational method for landslide emergency management: the Montaguto earthflow (AV, Italy)." *Nat. Hazards Earth Syst. Sci.*, 17, 845-860. https://doi.org/10.5194/nhess-17-845-2017.

Innovmetric, 2020. "PolyWorks web page." Accessed January 28, 2020. http://www.innovmetric.com/en,

Jaud, M., Passot, S., Le Bivic, R., Delacourt, C., Grandjean, P. and N. Le Dantec. 2016. "Assessing the Accuracy of High Resolution Digital Surface Models Computed by PhotoScan® and MicMac® in Sub-Optimal Survey Conditions." *Remote Sens.*, 8 (6), 465. https://doi.org/10.3390/rs8060465.

Lichti, D.D. and S. Jamtsho. 2006. "Angular resolution of terrestrial laser scanners. *Photogramm. Rec.*", 21 (114), 141–160. https://doi.org/10.1111/j.1477-9730.2006.00367.x.

Kastelic, V., Burrato, P., Carafa, M.M.C. and R. Basili. 2017. "Repeated surveys reveal nontectonic exposure of supposedly active normal faults in the central Apennines, Italy." *J. Geophys. Res.: Earth Surface*, 122, 114-129. https://doi.org/10.1002/2016JF003953.

Murtiyoso, A., Grussenmeyer, P., Börlin, N., Vandermeerschen, J. and T. Freville. 2018. "Open Source and Independent Methods for Bundle Adjustment Assessment in Close-Range UAV Photogrammetry." *Drones*, 2 (1), 3, 1-18. https://doi.org/10.3390/drones2010003.

Nouwakpo, S.K., Weltz, M.A. and K. McGwire. 2016. "Assessing the performance of structure-from-motion photogrammetry and terrestrial LiDAR for reconstructing soil surface

536 microtopography of naturally vegetated plots." *Earth Surf. Proc. Land.*, 41 (3), 308-322.
537 https://doi.org/10.1002/esp.3787.
538 Paredes-Hernandez, C.U., Salinas-Castillo, W.E., Guevara-Cortina, F. and X. Martinez-
539 Becerra. 2013. "Horizontal positional accuracy of Google Earth's imagery over rural areas: a
540 study case in Tamaulipas, Mexico." *Bol. de Ciênc. Geod.*, 19 (4), 588-601.
541 https://doi.org/10.1590/S1982-21702013000400005.
542 Pesci, A., Amoroso, S., Teza, G. and L. Minarelli. 2018. "Characterisation of soil deformation
543 due to blast-induced liquefaction by UAV-based photogrammetry and terrestrial laser
544 scanning." *Int. J. Remote Sens.*, 39 (22), 8317-8336.
545 https://doi.org/10.1080/01431161.2018.1484960.
546 Pesci, A., Teza, G., Bisson, M., Muccini, F., Stefanelli, P., Anzidei, M., Carluccio, R.,
547 Nicolosi, I., Galvani, A., Sepe, V. and C. Carmisciano. 2016. "A fast method for monitoring
548 the coast through independent photogrammetric measurements: application and case study."
549 *J. Geosci. Geomatics*, 4 (4), 73-81. https://doi.org/10.12691/jgg-4-4-1.
550 Pesci, A., Teza, G. and F. Loddo. 2019. "Low cost Structure-from-Motion-based fast
551 surveying of a rock cliff: precision and reliability assessment." Quad. Geofis. INGV, 156, 1-
552 22. ISSN: 1590-2595. Accessed February 14, 2020.
553 http://editoria.rm.ingv.it/quaderni/2019/quaderno156/.
554 Pesci, A., Teza, G. and E. Bonali. 2011. "Terrestrial laser scanner resolution: numerical
555 simulations and experiments on spatial sampling optimization." *Remote Sens.*, 3 (1), 167-184.
556 https://doi.org/10.3390/rs3010167.
557 Pulighe, G., Baiocchi, V. and F. Lupia. 2016. "Horizontal accuracy assessment of very high
558 resolution Google Earth images in the city of Rome, Italy." *Int. J. Dig. Earth*, 9 (4), 342-362.
559 https://doi.org/10.1080/17538947.2015.1031716.
560 Schlagenhauf, A. 2009. "Identication des forts séismes passés sur les failles normales actives
561 de la région Lazio-Abruzzo (Italie Centrale) par `datations cosmogéniques' (36Cl) de leurs

escarpements." PhD Thesis, Université Joseph-Fourier, Grenoble I, France, pp.1-299, in French. Accessed 11 October 2019. https://tel.archives-ouvertes.fr/tel-00461004.

Smith, M.W., Carrivick, J.L. and D.J. Quincey. 2016. "Structure from motion photogrammetry in physical geography." *Progr. Phys. Geography*, 60 (2), 247-275. https://doi.org/10.1177/0309133315615805.

Teza, G., Pesci, A. and A. Ninfo. 2016. "Morphological analysis for architectural applications: comparison between laser scanning and Structure-from-Motion photogrammetry." *J. Survey Eng.*, 142 (3): 04016004. https://doi.org/10.1061/(ASCE)SU.1943-5428.0000172.

Teza, G., Galgaro, A., Zaltron, N. and R. Genevois. 2007. "Terrestrial laser scanner to detect landslide displacement fields: a new approach." *Int. J. Remote Sens.*, 28 (16), 3425-3446. https://doi.org/10.1080/01431160601024234.

Tonkin, N.T. and G.N. Midgley. 2016. "Ground-Control Networks for Image Based Surface Reconstruction: An Investigation of Optimum Survey Designs Using UAV Derived Imagery and Structure-from-Motion Photogrammetry." *Remote Sens.*, 8 (9), 786. https://doi.org/10.3390/rs8090786.

Travelletti J., Delacourt C., Malet J.P., Allemand P., Schmittbuhl J. and R. Toussaint. 2013. "Performance of Image Correlation Techniques for Landslide Displacement Monitoring." In *Landslide Science and Practice*, edited by C. Margottini, P. Canuti, and K. Sassa, 217-226, Berlin, Heidelberg, D: Springer.

Triggs, B., Mclauchlan, P., Hartley, P. and A. Fitzgibbon. 2000. "Bundle Adjustment – A Modern Synthesis." In Proc., *International Workshop on Vision Algorithms IWVA 1999*, edited by B. Triggs, A. Zisserman and R. Szeliski, 298-372, Berlin, Heidelberg, D: Springer. https://doi.org/ 10.1007/3-540-44480-7_21.

586 Turner, D., Lucieer, A. and L. Wallace. 2014. “Direct georeferencing of ultrahigh-resolution
587 UAV imagery.” *IEEE T. Geosci. Remote Sens.*, 52 (5), 2738–2745.
588 https://doi.org/10.1109/TGRS.2013.2265295.
589 Vajsová, B., Walczynska, A., Aastrand, P., Barisch, S. and S. Hain, 2015. “New sensors
590 benchmark report on WorldView-3.” Brussels, B: Publications Office of the European Union.
591 Accessed February 14, 2020.
592 https://publications.jrc.ec.europa.eu/repository/bitstream/JRC99433/reqno_jrc99433_lb-na-
593 27673-en-n.pdf.
594

595 **Figure captions**

596

597 **Fig. 1**. Experiment with an artificial target: (a) target; (b) a point cloud; (c) a particular of the
598 point cloud; (d) selection of the dark points; (e) layout.

599

600 **Fig. 2**. Results of preliminary experiment with an artificial target: ground sampling distance
601 (GSD), i.e. pixel size, and point cloud resolution vs. acquisition distance for a focal length (*f*)
602 of (a) 55 mm; (b) 102 mm; (c) 210 mm; (d) ratio between resolution and GSD vs. acquisition
603 distance; (e) GSD and point cloud resolution vs. distance normalized for f = 55 mm.

604

605 **Fig. 3**. Campo Felice bedrock scarp: (a) general tectonic setting of the central Apennines. The
606 lines stand for active faults mapped on the basis of geomorphic characteristics (Schlagenhauf
607 2009) and the star marks the position of the bedrock scarp; (b) image of the surveyed
608 mountain slope with the exposed bedrock scarp; (c) geologic and morphologic characteristics
609 of the mountain slope.

610

611 **Fig. 4**. TLS-based survey: (a) vertical point cloud cross section and slope inclination; (b)
612 frontal perspective view of the central part of the surveyed slope. A distance between two
613 points of the cloud provide an immediate scale for the surveyed area.

614

615 **Fig. 5**. SfM-based survey: (a) point cloud obtained from images with 55 mm *f*, where the lines
616 indicate the boundaries of the areas modelled for the used *f* values; (b), (c), (d) sample images
617 taken with *f* of 220 mm, 110 mm e 55 mm respectively; (e) camera positions and orientations
618 with respect to the observed cliff in the case of 55 mm *f*.

619

Fig. 6. Maps of differences between the pairs of point clouds related to focal length of 55 mm (a), 110 mm (b) and 200 mm (c). Maps of differences between point clouds related to different focal lengths: (d) 55 mm vs. 110 mm; (e) 55 mm vs. 220 mm; (f) 110 mm vs. 220 mm.

Fig. 7. Distributions of differences between pairs of point clouds. Pairs related to the same focal length: (a) 55 mm, (b) 110 mm and (c) 220 mm; pairs related to different focal lengths: (d) 55 mm vs. 110 mm; (e) 55 mm vs. 220 mm; (f) 110 mm vs. 220 mm. For each distribution of observational data, the corresponding normal distribution with the same parameters is also shown.

Fig. 8. Multitemporal data comparison for a focal length of 110 mm: (a) 2019 point cloud, on which the boundary of 2018 point cloud is shown; (b) 2018 point cloud; (c) 2018-2019 differences in the range ±0.1 m; (d) 2018-2019 differences in the range outside the resolution limit (0.04 m); (e) 2018-2019 differences inside the range ±0.04 m.

Fig. 9. SfM and TLS point clouds comparison: difference maps for focal length of (a) 55 mm, (b) 110 mm and (c) 220 mm; (d) TLS and 55 mm SfM point clouds.

Table 1. Camera technical specifications.

Feature/parameter	Unit	Value
Camera	-	Nikon D3300
Focal length	mm	55-300
Crop factor	-	1.5
Equivalent focal length 35 mm	mm	83-450
Sensor number of pixels	-	6000 x 4000
Sensor size	mm x mm	23.5 x 15.6
Pixel size	mm	0.0039
Aperture (f-stop)	-	*f*/8
Sensibility	ISO	400

Table 2. Some details about the PhotoScan data processing

Survey			Number of tie points	Number of points (10^6)	Computation time (h)		
f (mm)	#	Images taken			Camera alignment	Dense point cloud generation	Total
55	1	30	1071	21.140	0.08	0.82	0.90
55	2	30	1133	21.250	0.08	0.82	0.90
110	1	42	1906	39.950	0.12	3.33	3.50
110	2	42	1880	40.570	0.12	3.33	3.50
220	1	44	2656	50.960	0.15	3.65	3.80
220	2	44	2750	47.410	0.15	3.65	3.80

Note: The computation times are referred to a notebook equipped by an Intel Core i7, 2.40 GHz CPU and 16 Gb RAM

Table 3. Main statistical parameters of data comparisons

Point cloud (*f*, mm)	U/B [1]	Mean (m)	Median (m)	SD (σ, m)	skewness	kurtosis
55	B	0.006	-0.005	0.018	-0.26[a]	35[a]
110	U	-0.001	-0.002	0.012	0.34	20
220	U	-0.001	-0.001	0.007	0.30	41
55-110	B	0.002	0.003	0.031	-0.96[a]	18[a]
55-220	B	0.023	0.025	0.034	0.24[a]	5.6[a]
110-220	U	0.001	0.002	0.016	-1.0	4.1

Note: U: unimodal distribution; B: bimodal distribution.

[a] Since the distribution is bimodal, the values of skewness and kurtosis are not significant.

Figure 1

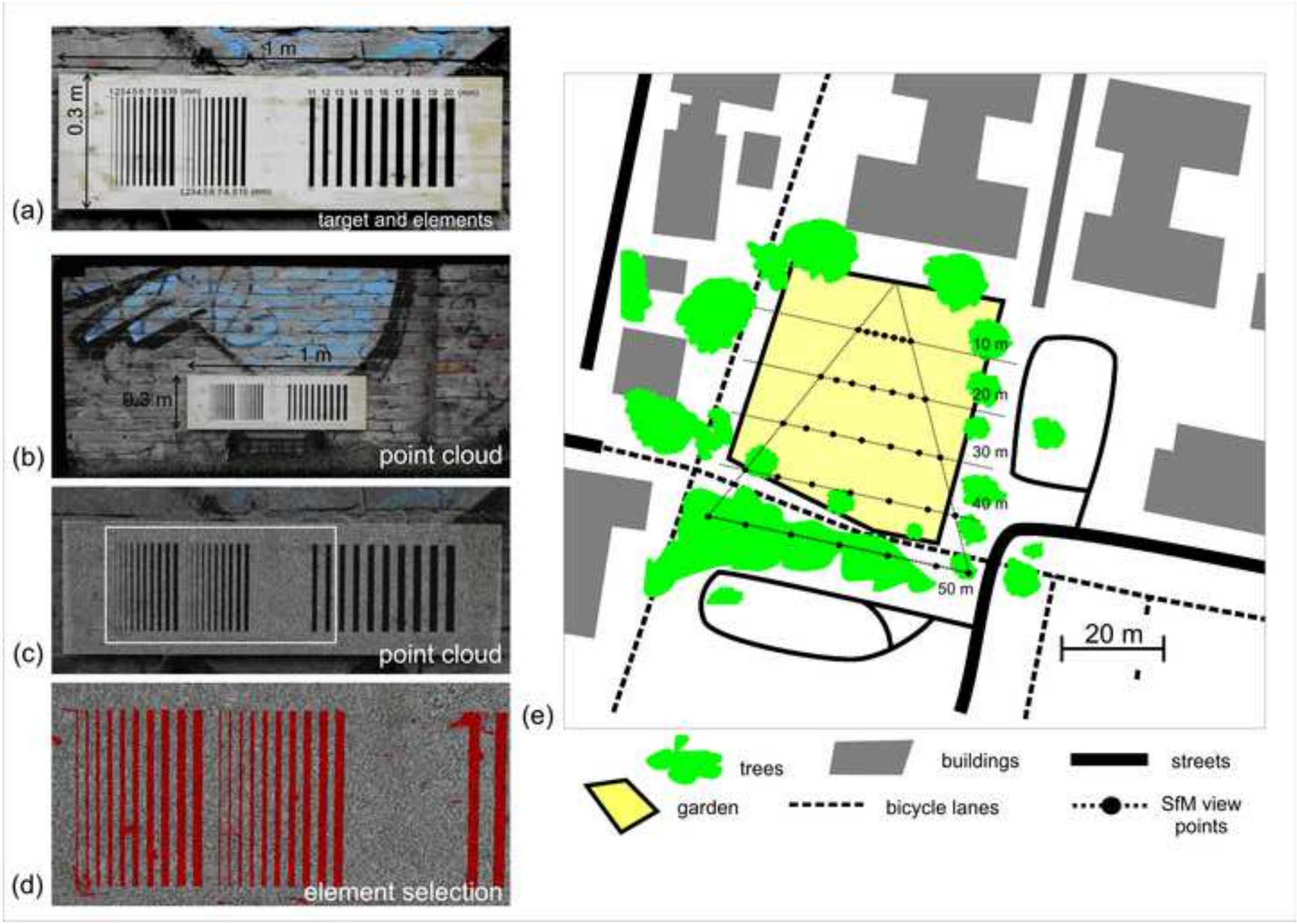

Figure 2

Click here to access/download;Figure;Fig_2.tif

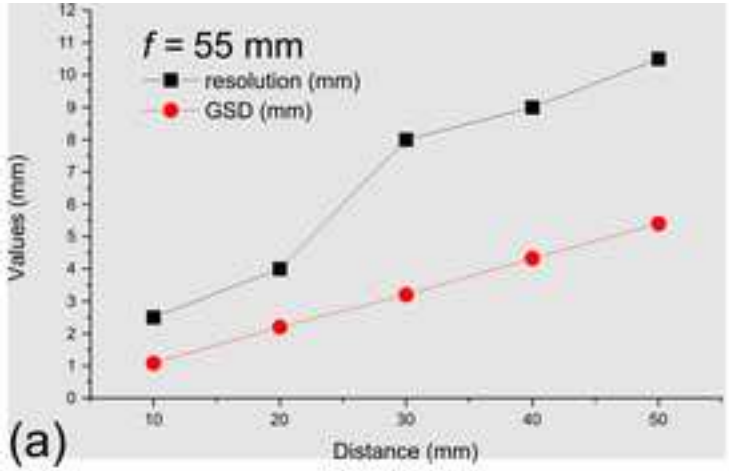

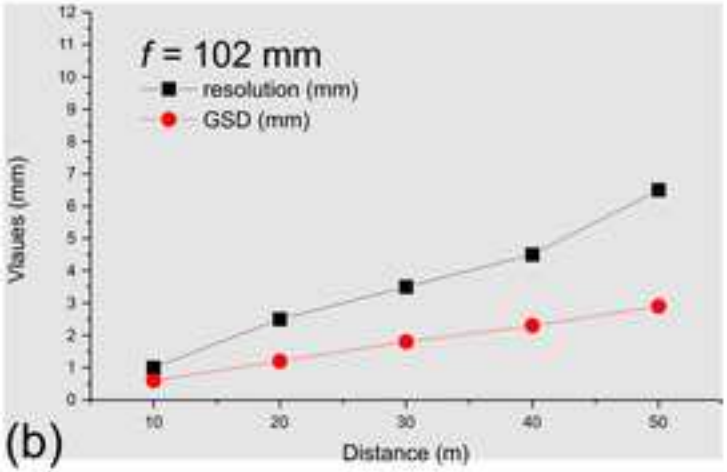

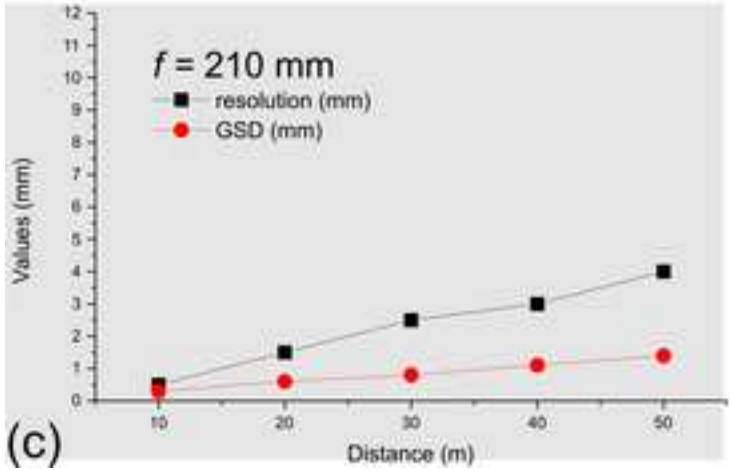

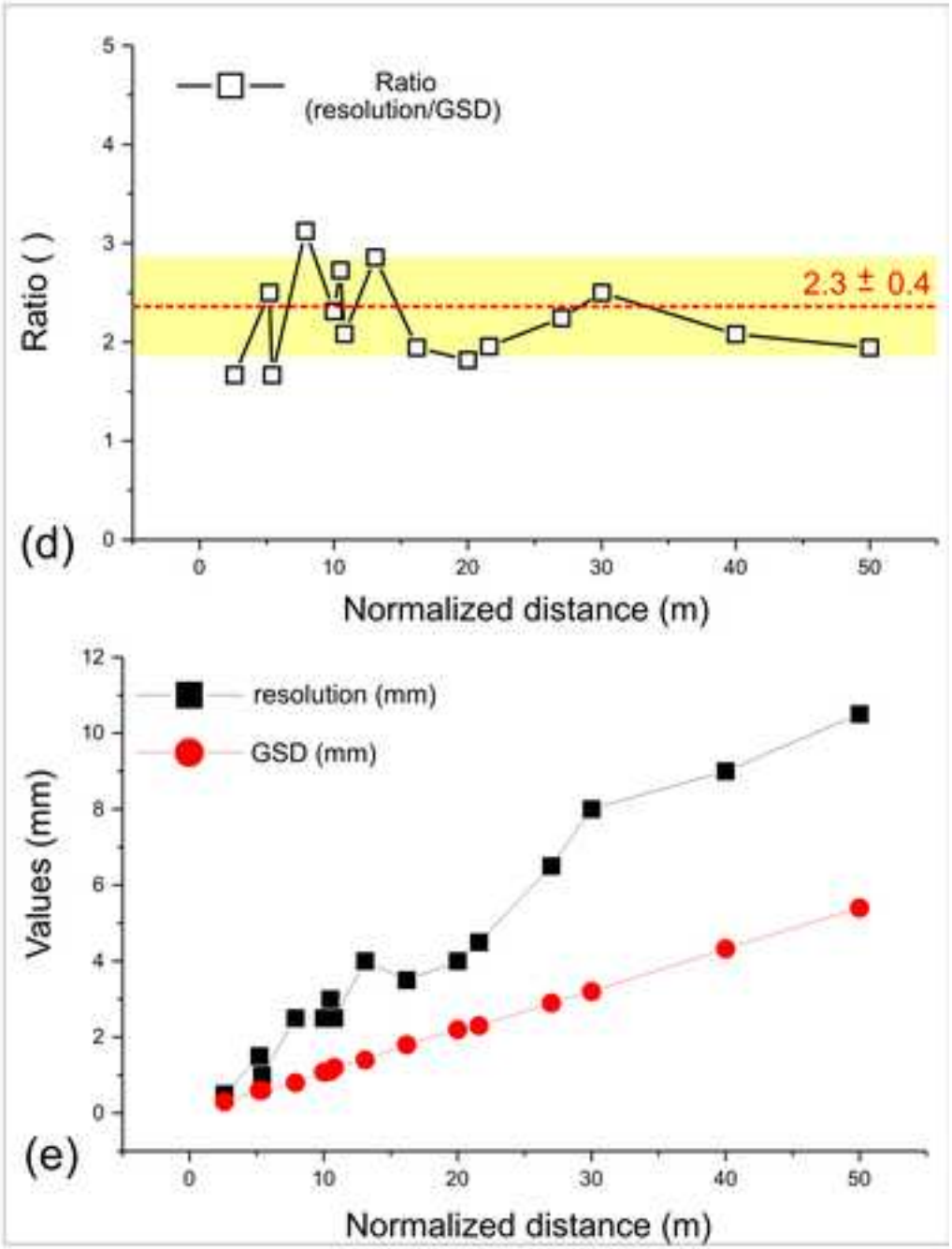

Figure 3

Click here to access/download;Figure;Fig_3.tif

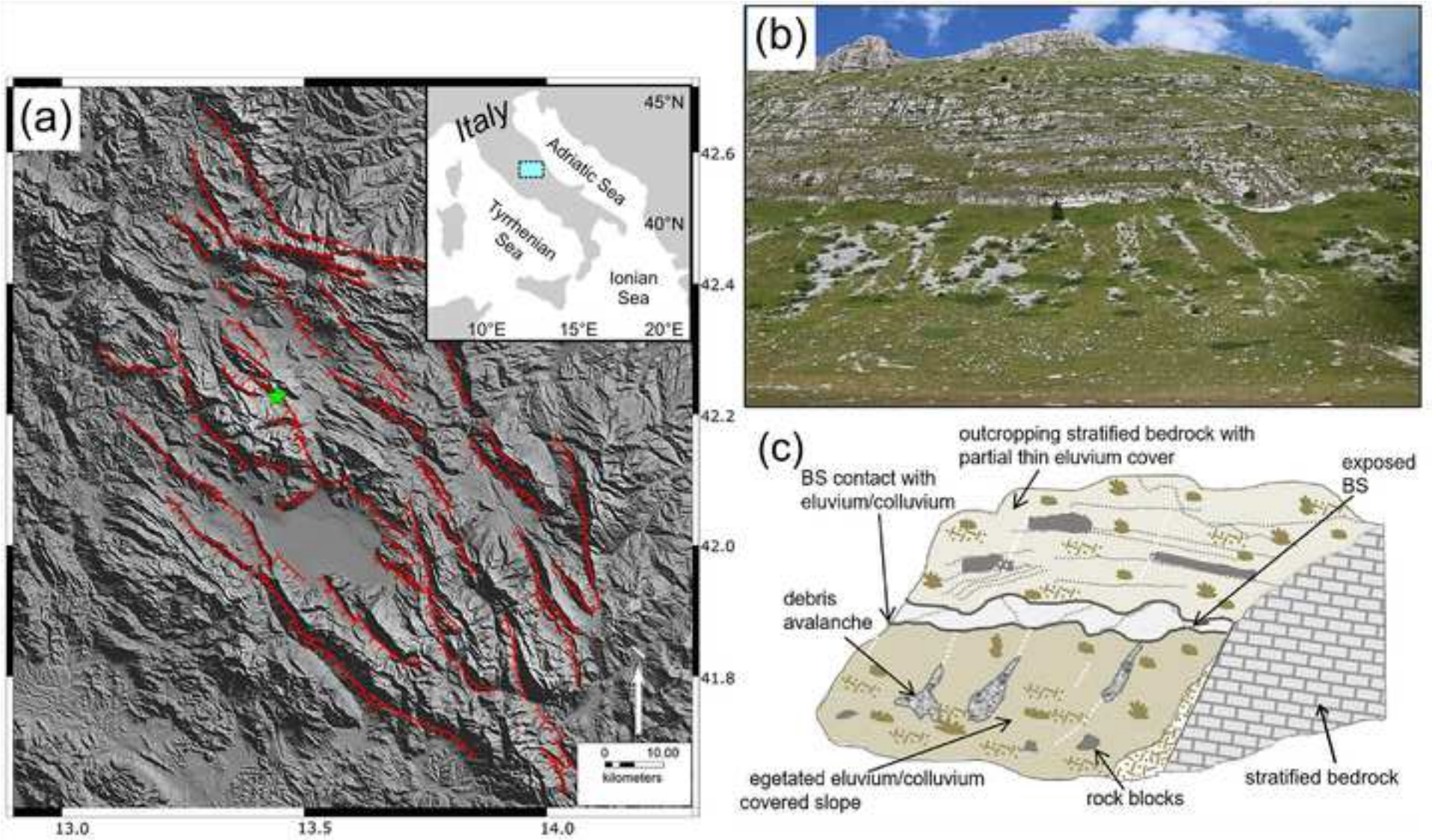

Figure 4

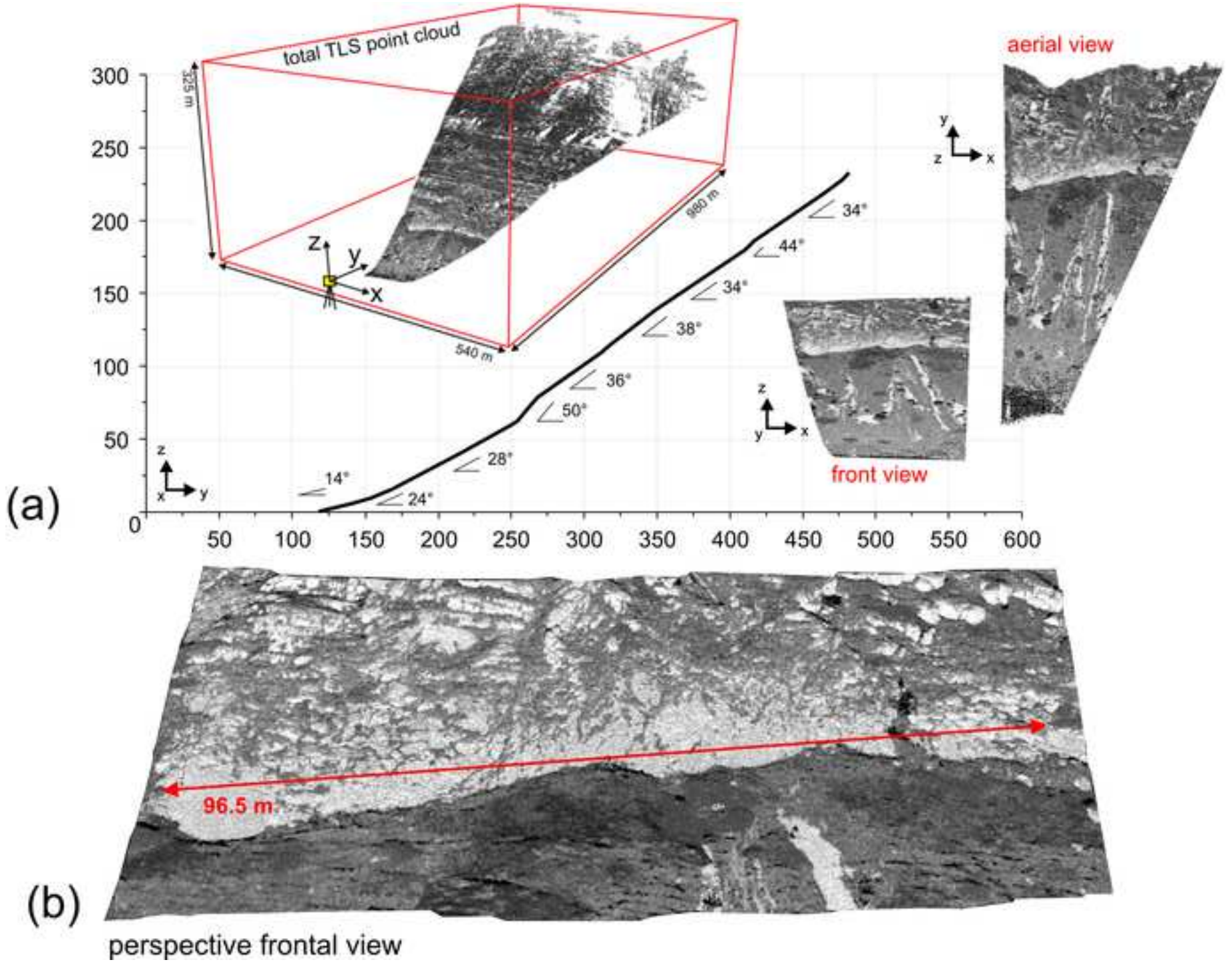

Figure 5

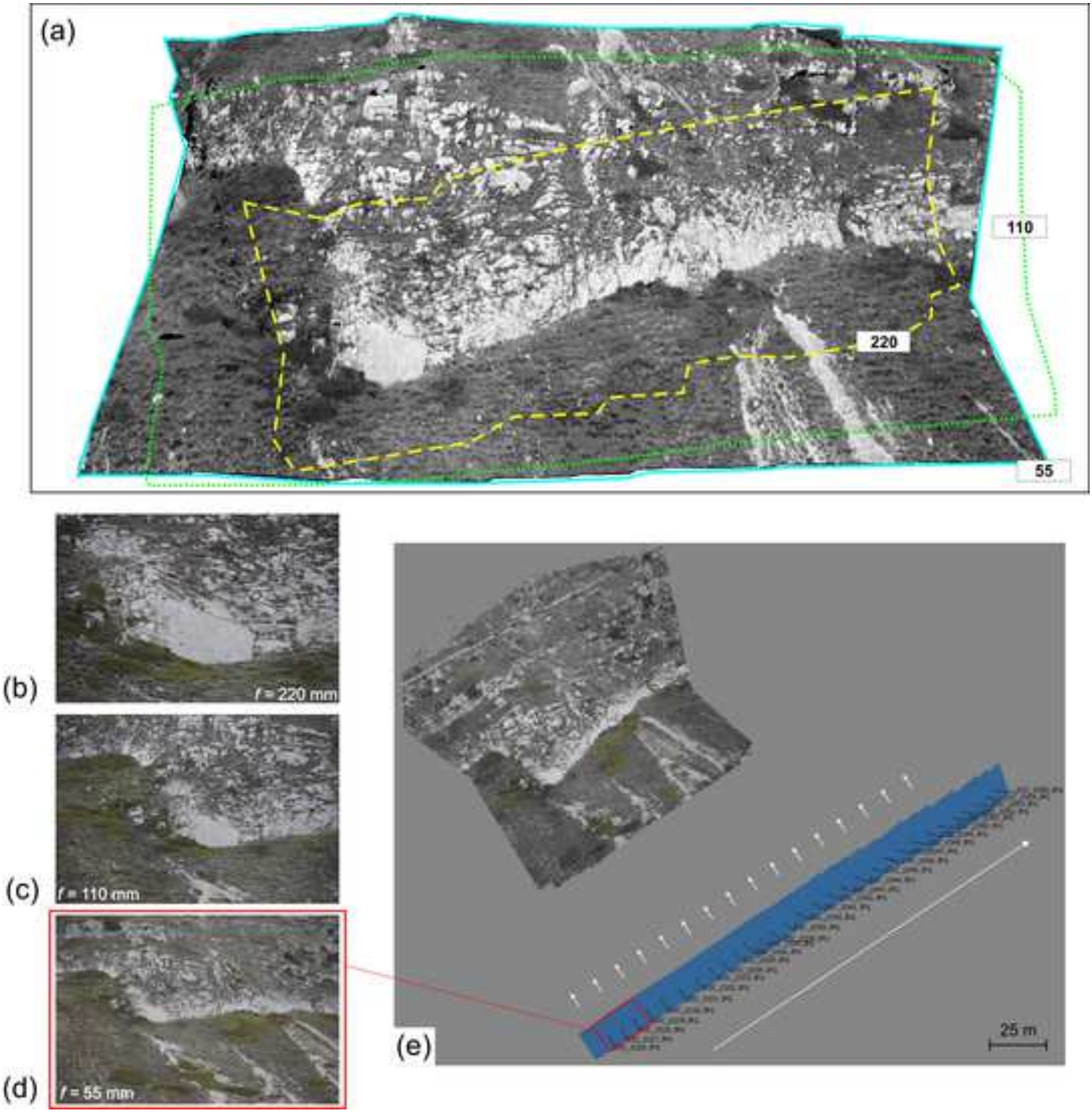

Figure 6

Click here to access/download;Figure;Fig_6.tif

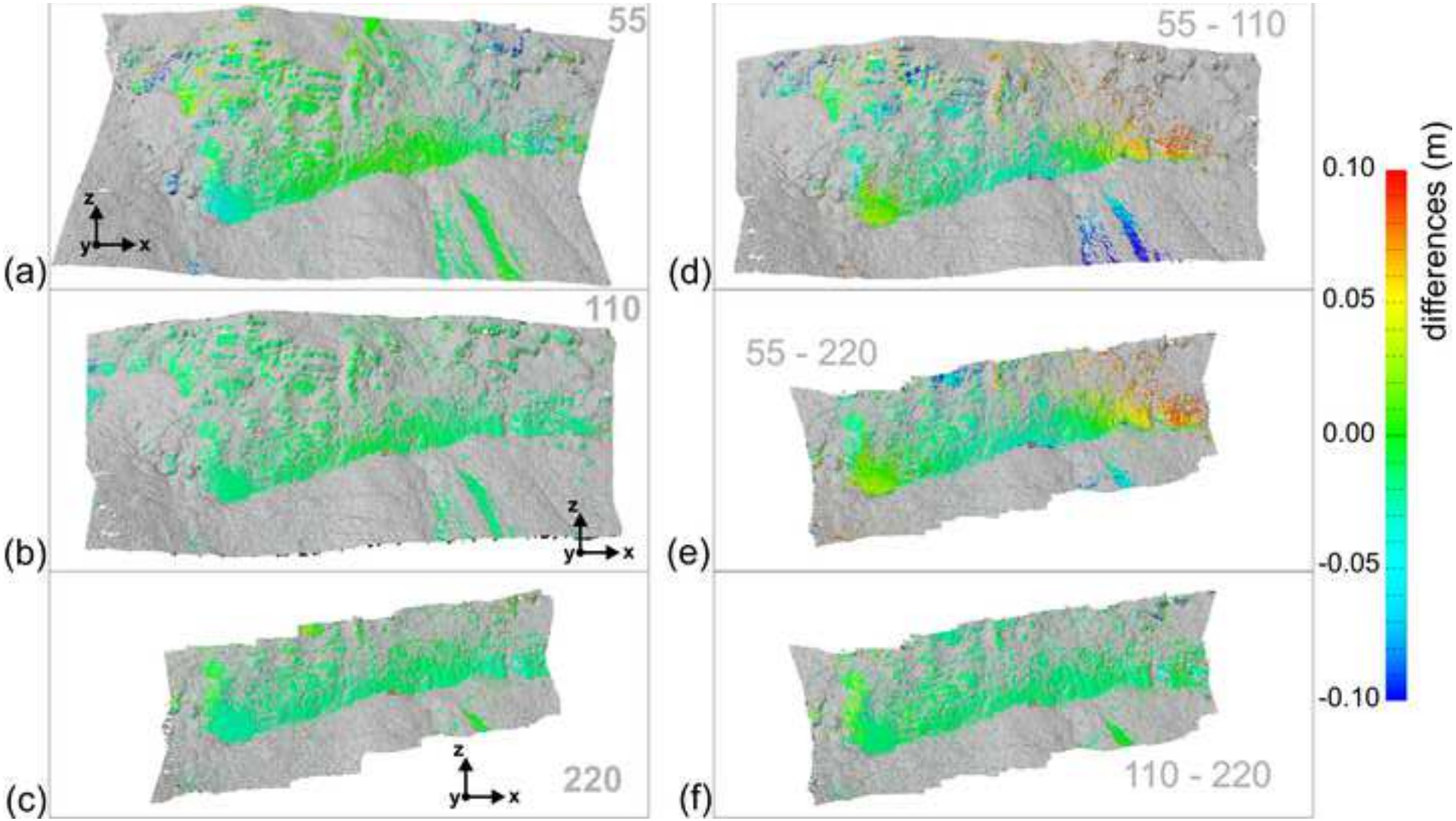

Figure 7

Click here to access/download;Figure;Fig_7.tif

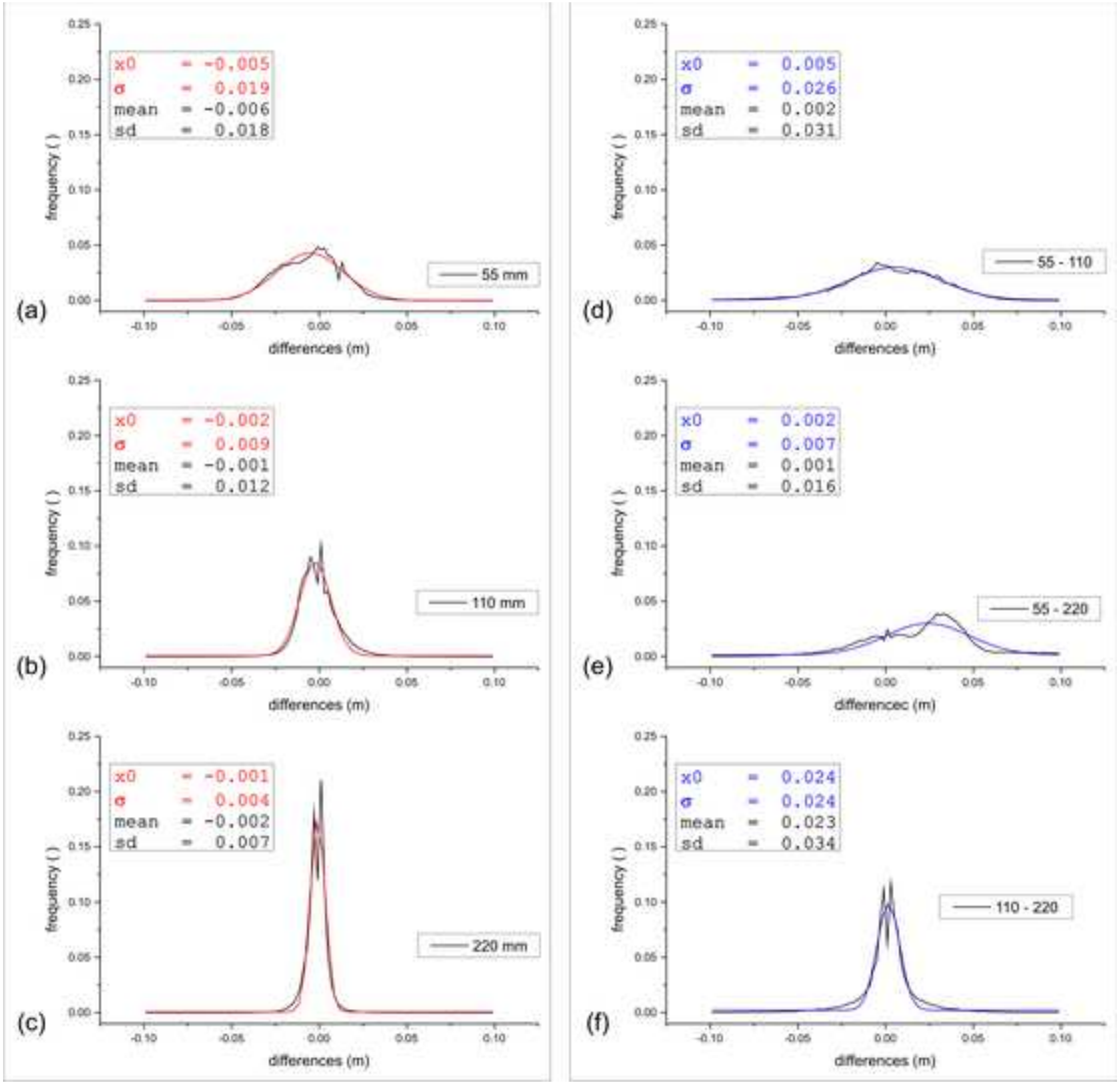

Figure 8

Click here to access/download;Figure;Fig_8.tif

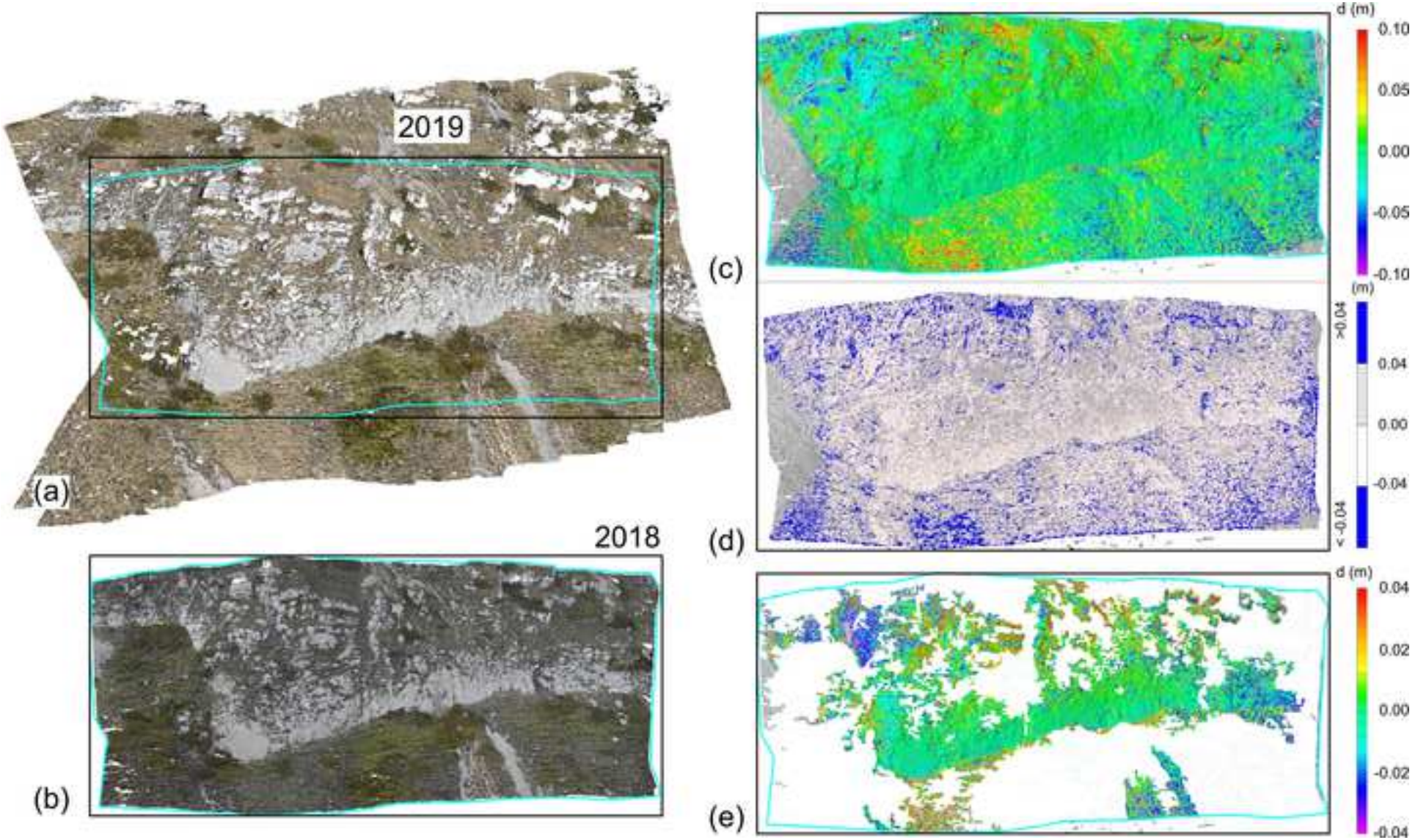

Figure 9

Click here to access/download;Figure;Fig_9.tif